Weierstraß-Institut
für Angewandte Analysis und Stochastik

Leibniz-Institut im Forschungsverbund Berlin e. V.

Preprint ISSN 2198-5855

On the spinodal dewetting of thin liquid bilayers

Roghayeh Shiri[1], Leonie Schmeller[2],

Ralf Seemann[1], Dirk Peschka[2], Barbara Wagner[2]

submitted: July 23, 2021

[1] Department of Experimental Physics
Saarland University
66123 Saarbrücken
Germany
E-Mail: roghayeh.shiri@physik.uni-saarland.de
r.seemann@physik.uni-saarland.de

[2] Weierstrass Institute Berlin
Mohrenstr. 39
10117 Berlin
Germany
E-Mail: leonie.schmeller@wias-berlin.de
dirk.peschka@wias-berlin.de
barbara.wagner@wias-berlin.de

No. 2861
Berlin 2021

2020 *Mathematics Subject Classification.* 35R35, 76A20, 76E17.

2010 *Physics and Astronomy Classification Scheme.* 68.05.Cf, 68.37.Ps, 68.03.Cd.

Key words and phrases. spinodal decomposition, thin-film, bilayer, white noise, coloured noise.

LS, RS, RS, DP and BW acknowledge the financial by the German Research Foundation (DFG) through the projects #422786086 and #422792530 within the DFG Priority Program *SPP 2171* and through the projects #167121686 within the DFG Priority Program *SPP 1506*.

Edited by
Weierstraß-Institut für Angewandte Analysis und Stochastik (WIAS)
Leibniz-Institut im Forschungsverbund Berlin e. V.
Mohrenstraße 39
10117 Berlin
Germany

Fax: +49 30 20372-303
E-Mail: preprint@wias-berlin.de
World Wide Web: http://www.wias-berlin.de/

On the spinodal dewetting of thin liquid bilayers

Roghayeh Shiri, Leonie Schmeller,

Ralf Seemann, Dirk Peschka, Barbara Wagner

Abstract

We investigate the spinodal dewetting of a thin liquid polystyrene (PS) film on a liquid polymethylmethacrylate (PMMA) subtrate. Following the evolution of the corrugations of the PS film via in situ measurements by atomic force microscopy (AFM) and those of the PS-PMMA interface via ex situ imaging, we provide a direct and detailed comparison of the experimentally determined spinodal wavelengths with the predictions from linear stability analysis of a thin-film continuum model for the bilayer system. The impact of rough interfaces and fluctuations is studied theoretically by investigating the impact of different choices of initial data on the unstable wavelength and on the rupture time. The key factor is the mode selection by initial data perturbed with correlated colored noise in the linearly unstable regime, which becomes relevant only for liquid bilayers to such an extent. By numerically solving the mathematical model, we further address the impact of nonlinear effects on rupture times and on the morphological evolution of the interfaces in comparison with experimental results.

1 Introduction

Flows of viscous fluids with free surfaces have been studied for many decades and are critical to many applications [1]. Dewetting processes are of particular interest because they generate flows that lead to interesting physical phenomena and reveal fundamental mathematical challenges, e.g., moving contact line problem [2, 3] and stability and pattern formation in free surface flows [4]. Dewetting flows with moving interfaces and moving contact lines on solid substrates [5, 6] and on liquid substrates [7] have been studied extensively over the years [5, 6] and continue to provide many fundamental insights. Thus, the dewetting from soft or liquid substrates is not only relevant for its many applications but also for its use to address fundamental physical questions.

In many ways, the dewetting of a viscous liquid from another immiscible viscous substrate is similar to that on a solid substrate: When a uniform layer is energetically unfavorable, then a thin liquid layer will destabilize either spinodally or by heterogeneous nucleation [8–14]. Driven by surface energies, resulting holes will grow over time and lead to characteristic dewetting rims that ultimately lead to arrays of stationary droplets [15, 16]. However, dewetting from a liquid substrate is also strikingly different and thus fundamentally interesting: Firstly, the existence of a liquid substrate naturally cures the contact line singularity and thereby provides an ideal modeling system to study interfacial and contact line dynamics – in that respect de Gennes called liquid substrates the *epitome of perfection* [17, pg. 169]. Secondly, the interaction of the viscous flow through the polymer-polymer interface leads to a nontrivial coupling of dissipative processes in the flow and in the substrate that can potentially affect dewetting and pattern formation processes [18, 19]. This coupling provides additional complexity and leads to many alternative pathways in early and late stages of the dewetting process and is only relatively well understood theoretically in the classical linear regime [11].

DOI 10.20347/WIAS.PREPRINT.2861 Berlin 2021

For a polymer-polymer system on a solid substrate one first needs to understand the destabilization of initially thin flat polymer layers, as this instability will affect the entire subsequent dewetting process. The initial period of the polymer-polymer spinodal dewetting was investigated experimentally using neutron reflection measurements [20] and theoretically using linear stability analysis [11] and by numerical simulations [12, 21]. It was shown that by changing the thickness ratio of the layers one can switch between different dominant instability modes, i.e., so-called “varicose” and “zig-zag” modes. Extensions to interfacial slip and its impact on the instability have been investigated in [22], surfactant-driven flows have been investigated in [23, 24], more complex energetic models with sharp moving contact lines have been developed in [25]. Later stages of the evolution have been studied using AFM measurements of interface shapes, e.g., [26].

Finally, spatio-temporal fluctuations as considered in the works by Davidovitch et al. [27] and Grün et al. [28] have been found relevant to explain discrepancies of time-scales for spinodal nucleation for thin-films on solid substrates. Since all the underlying models are aligned with the fluctuation-dissipation theorem, a consistent extension to multi-layered thin-film system should involve a nontrivial coupling of fluctuations of the PS-air interface and of the PS/PMMA interface. This study will also motivate the usefulness of such an extension to further understand the spinodal instability of polymer-polymer systems due to the presence of possibly correlated colored noise and fluctuations.

In this study we revisit the spinodal dewetting of a polymer-polymer system and investigate the onset of the evolution by direct AFM measurements and provide a detailed comparison with the linear theory and compare with nonlinear simulations. Therefore, in 2 we provide the corresponding experimental and theoretical methodology, characterize the experimental setup, and present the used polymer system. In 3 we will then investigate the spinodal dewetting by comparing the general evolution of measured AFM profiles and of power spectral densities with predictions by the underlying linear and nonlinear theory.

2 Experimental and Theoretical Methods

2.1 Model and linear stability

Thin-film model. In the following we review theoretical facts that are relevant for the understanding of the spinodal dewetting of liquid-liquid thin films. Consider a two layer system with a liquid polystyrene film (PS) on top of a liquid polymethylmethacrylate substrate (PMMA) as sketched in Figure 1. The solid-liquid interface is located at $z = 0$, the liquid-liquid (PS-PMMA) interface is at $z = h_{\mathrm{PMMA}}(t, \boldsymbol{x})$, and the liquid-air (PS-air) is at $z = h(t, \boldsymbol{x}) = h_{\mathrm{PMMA}}(t, \boldsymbol{x}) + h_{\mathrm{PS}}(t, \boldsymbol{x})$ for time $t > 0$ and at points $\boldsymbol{x} \in \mathbb{R}^2$, respectively. The viscosity of the PS and PMMA phase are denoted by μ_α for $\alpha \in \{\mathrm{PS}, \mathrm{PMMA}\}$ and the surface tensions of the PS-air and PS-PMMA interface by γ_ℓ for $\ell \in \{\text{PS-air}, \text{PS-PMMA}\}$. The flow of both Newtonian liquids is governed by the incompressible Navier-Stokes equation with free capillary boundaries and is driven by intermolecular potentials $\Phi(h)$ that destabilize the PS layer and lead to spinodal dewetting [22, 29].

The basis of the theory is a thin-film model, which emerges from the original Navier-Stokes free boundary problem by an asymptotic long-wavelength approximation [23]. First, one introduces a nondimensionalization using typical parameters for pressure, length and velocity

$$P = \tfrac{2n}{n-2}\tfrac{\phi_*}{H}, \quad L = \sqrt{\tfrac{\gamma_{\text{PS-air}} H}{P}}, \quad U = \tfrac{PH^2}{\mu_{\mathrm{PS}} L} = \tfrac{L}{T},$$

so that the aspect ratio is small, i.e., $\varepsilon = H/L \ll 1$.

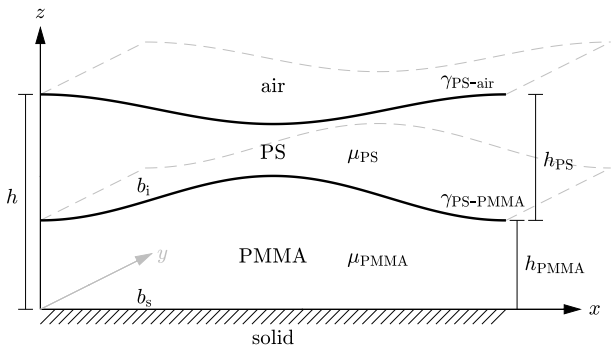

Figure 1: Sketch of PS-PMMA system with free PS-air interface at $h = h_{\text{PS}} + h_{\text{PMMA}}$ and PS-PMMA interface at h_{PMMA}.

Introducing the non-dimensional surface tension ratio $\gamma = \gamma_{\text{PS-PMMA}}/\gamma_{\text{PS-air}}$, the two-layer thin film system is modelled using the energy functional

$$\mathcal{E}(\boldsymbol{h}) = \int_\Omega \frac{\gamma}{2}|\nabla h_{\text{PMMA}}|^2 + \frac{1}{2}|\nabla h|^2 + \Phi(h_{\text{PS}})\,\mathrm{d}\boldsymbol{x}. \tag{2.1a}$$

where $\boldsymbol{h}(t,\boldsymbol{x}) = \big(h_{\text{PMMA}}(t,\boldsymbol{x}), h_{\text{PS}}(t,\boldsymbol{x})\big)$ and the total height $h = h_{\text{PS}} + h_{\text{PMMA}}$. The evolution for the layer heights $\boldsymbol{h}$ is then governed by the thin-film equation

$$\partial_t \boldsymbol{h} = \nabla \cdot \Big[\boldsymbol{Q}(\boldsymbol{h})\nabla\frac{\delta\mathcal{E}}{\delta\boldsymbol{h}}\Big], \tag{2.1b}$$

with $\frac{\delta\mathcal{E}}{\delta\boldsymbol{h}} = (\frac{\delta\mathcal{E}}{\delta h_{\text{PMMA}}}, \frac{\delta\mathcal{E}}{\delta h_{\text{PS}}})$. The degenerate mobility matrix $\boldsymbol{Q}(\boldsymbol{h}) = \boldsymbol{Q}_{\text{visc}}(h_{\text{PMMA}}, h_{\text{PS}}) + \boldsymbol{Q}_{\text{slip}}(h_{\text{PMMA}}, h_{\text{PS}})$ encodes viscous dissipation and Navier slip at the interfaces

$$\boldsymbol{Q}_{\text{visc}}(u,v) = \frac{1}{\mu}\begin{pmatrix} \frac{u^3}{3} & \frac{u^2 v}{2} \\ \frac{u^2 v}{2} & \frac{\mu}{3}v^3 + uv^2 \end{pmatrix}, \tag{2.2a}$$

$$\boldsymbol{Q}_{\text{slip}}(u,v) = b_{\text{s}}\begin{pmatrix} u^2 & uv \\ uv & v^2 + (\mu+1)\frac{b_{\text{i}}}{b_{\text{s}}}v^2 \end{pmatrix}, \tag{2.2b}$$

where $\mu = \mu_{\text{PMMA}}/\mu_{\text{PS}}$ is the viscosity ratio, b_{s} and b_{i} are the Navier slip length at the solid-PMMA surface and the PS-PMMA interface [12, 22], respectively. We discretize the thin-film problem (2.1b) using finite elements by seeking $\boldsymbol{h}^n = \boldsymbol{h}(t^n,\boldsymbol{x}), \boldsymbol{\pi} = \boldsymbol{\pi}(t^n,\boldsymbol{x})$ such that

$$\int_\Omega \frac{\boldsymbol{h}^n - \boldsymbol{h}^{n-1}}{\tau}\cdot\boldsymbol{v} + \boldsymbol{Q}(\boldsymbol{h}^{n-1})\nabla\boldsymbol{\pi}\cdot\nabla\boldsymbol{v}\,\mathrm{d}\boldsymbol{x} = 0, \tag{2.3a}$$

$$\int_\Omega \boldsymbol{\pi}\cdot\boldsymbol{w} - \boldsymbol{w}\cdot\left(\frac{\delta\mathcal{E}}{\delta\boldsymbol{h}}\right)^n \mathrm{d}\boldsymbol{x} = 0, \tag{2.3b}$$

for all suitable test functions $\boldsymbol{v} = (v_{\text{PMMA}}, v_{\text{PS}}), \boldsymbol{w} = (w_{\text{PMMA}}, w_{\text{PS}})$ and all natural boundary conditions. For the derivative of the energy we have

$$\left(\frac{\delta\mathcal{E}}{\delta\boldsymbol{h}}\right)^n = \begin{pmatrix} -(\gamma+1)\nabla^2 h_{\text{PMMA}} - \nabla^2 h_{\text{PS}} \\ -\nabla^2 h_{\text{PMMA}} - \nabla^2 h_{\text{PS}} + \Phi'(h_{\text{PS}}) \end{pmatrix}, \tag{2.4}$$

all evaluated at time $t^n = n\tau$ for $n \in \mathbb{N}$ and for given initial data $\boldsymbol{h}^0$. We use finite elements implemented in MATLAB and deal.II [30] to solve this problem numerically.

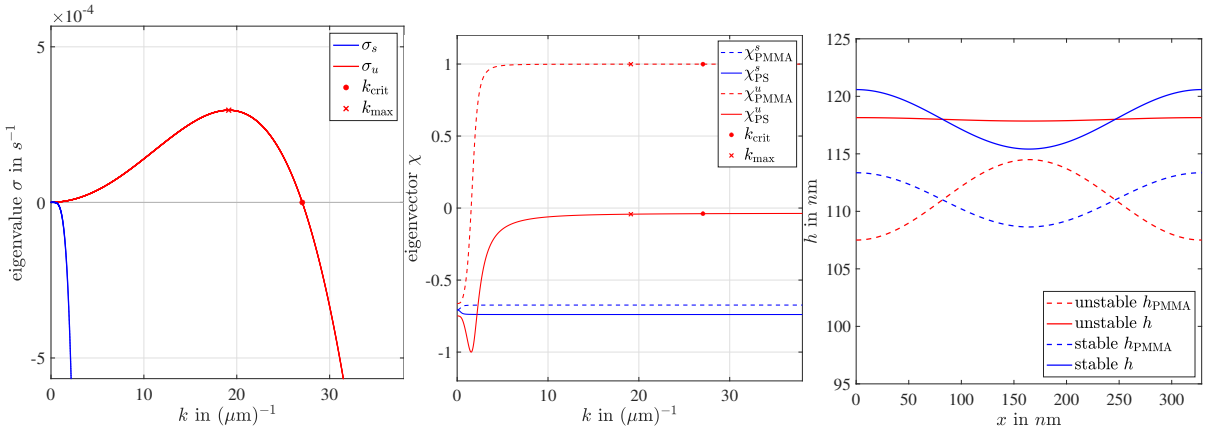

Figure 2: **(left)** Eigenvalues $\sigma_{s,u}(k)$ of stable and unstable branch. **(center)** Eigenvector $\boldsymbol{\chi}_{s,u}$ for the stable and unstable branch with $\chi_h = \chi_{\mathrm{PS}} + \chi_{\mathrm{PMMA}}$. **(right)** Initial perturbation $\boldsymbol{h} = \boldsymbol{h}^0 + \delta\boldsymbol{\chi}_\alpha \cos(k_x x)\cos(k_y y)$ using an unstable or stable eigenmode for $h^0_{\mathrm{PMMA}} = 111\,n\mathrm{m}$ and $h^0_{\mathrm{PS}} = 7\,n\mathrm{m}$ (amplitude exaggerated) for $k = k_{\max}$ using the physical parameters of the PS-PMMA system.

Linear stability. While the nonlinear evolution problem (2.1b) is solved to explore later stages of the spinodal dewetting, the onset of the instability is explored by a linear stability analysis. Starting from an initially flat film with given thicknesses $\boldsymbol{h}^0 = (h^0_{\mathrm{PMMA}}, h^0_{\mathrm{PS}}) \in \mathbb{R}^2$, we assume small perturbations of the form

$$\boldsymbol{h}(t,\boldsymbol{x}) = \boldsymbol{h}^0 + \delta\boldsymbol{\chi}(\boldsymbol{k})\cos(k_x x)\cos(k_y y)e^{\sigma(\boldsymbol{k})t} \tag{2.5a}$$

with $\boldsymbol{k} = (k_x, k_y)$, $\boldsymbol{x} = (x, y)$, and $\boldsymbol{\chi} = (\chi_{\mathrm{PMMA}}, \chi_{\mathrm{PS}})$ with $|\boldsymbol{\chi}| = 1$ in the linear regime for sufficiently small $0 < \delta \ll 1$. Plugging this ansatz into the dimension-reduced lubrication equation (2.1b), one obtains the usual nondimensional eigenvalue problem [11]

$$\sigma\boldsymbol{\chi} = -k^2\boldsymbol{Q}(\boldsymbol{h}^0)\boldsymbol{E}\boldsymbol{\chi}, \quad \boldsymbol{E} = \begin{bmatrix} (\gamma+1)k^2 & k^2 \\ k^2 & k^2 + \Phi''(h^0_{\mathrm{PS}}) \end{bmatrix},$$

with $k^2 = |\boldsymbol{k}|^2$ and $\det \boldsymbol{E} = 0$ at $k_{\mathrm{crit}} L = (\frac{\gamma+1}{\gamma})^{1/2}$. For $\boldsymbol{M} = \boldsymbol{Q}(\boldsymbol{h}^0)\boldsymbol{E}$ the k-dependent eigenvalues

$$\sigma_{s,u} = -\tfrac{1}{2}k^2 \operatorname{tr}(\boldsymbol{M}) \pm k^2\sqrt{\tfrac{1}{4}\operatorname{tr}(\boldsymbol{M})^2 - \det(\boldsymbol{M})}, \tag{2.5b}$$

have two branches which we call unstable σ_u and stable σ_s as shown in Figure 2. While $\sigma_s \le 0$ for all k, we have $\sigma_u > 0$ for $0 < k < k_{\mathrm{crit}}$ and $\sigma_u \le 0$ for $k > k_{\mathrm{crit}}$. Correspondingly, we have the eigenvectors $\boldsymbol{\chi}_{s,u} = (\chi^{s,u}_{\mathrm{PMMA}}, \chi^{s,u}_{\mathrm{PS}})$ which determine the components of $\boldsymbol{\chi}$ that are exponentially amplified or damped with $\sigma_{s,u}$. Thus, in the linear regime the evolution of general initial perturbations $\delta\boldsymbol{h}$ is given by the Fourier series in $\boldsymbol{k}$ with stable and unstable modes $m \in \{s, u\}$, i.e.,

$$\boldsymbol{h}(t,\boldsymbol{x}) = \boldsymbol{h}^0 + \sum_{\boldsymbol{k},m} \boldsymbol{w}_m \cos(k_x x)\cos(k_y y)e^{\sigma_\alpha t}, \tag{2.5c}$$

where $\boldsymbol{w}_m(\boldsymbol{k}) = (w^m_{\mathrm{PMMA}}, w^m_{\mathrm{PS}}) = (\delta\boldsymbol{h}\cdot\boldsymbol{\chi}_m)\,\boldsymbol{\chi}_m$. Hence, stable perturbations will quickly die out and the initial evolution will be dominated by unstable modes with $0 \le k \le k_{\mathrm{crit}}$. Correspondingly, the spinodal rupture time t_{rup} for given initial data is given by setting $h_{\mathrm{PS}} = 0$ in (2.5c), i.e.,

$$t_{\mathrm{rup}} = \frac{1}{\sigma_u}\log\left(\frac{h^0_{\mathrm{PS}}}{w^u_{\mathrm{PS}}}\right), \tag{2.5d}$$

and therefore also depends on the overlap of the initial perturbation $\delta\boldsymbol{h}$ with the unstable mode $\boldsymbol{\chi}_u$ and on $\boldsymbol{k}$. This dependence on the overlap is not present for single layer thin films, since the linear stability only features a single unstable branch. Usually the fastest growing mode

$$\sigma_{\max} = \sigma_u(k_{\max}) = \operatorname{argmax}_{\boldsymbol{k}} \sigma_u(\boldsymbol{k}), \tag{2.5e}$$

determines the rupture time $t \sim (\sigma_{\max})^{-1}$, if $\boldsymbol{w}_u$ does not or only weakly depends on $\boldsymbol{k}$.

2.2 Sample Preparation and AFM measurements

In order to monitor the dewetting of the liquid PS film from the liquid PMMA substrate, we use an experimental setup consisting of a nanometric thin polystyrene (PS) film with molecular weight of $63\,\mathrm{kg\,mol^{-1}}$ on top of an also nanometric film of polymethylmethacrylate (PMMA) with molecular weight of $10\,\mathrm{kg\,mol^{-1}}$. The glass transition temperature of PSÂă(63k) is $T_{\mathrm{G,PS}} = (95 \pm 5)°\mathrm{C}$, while that of PMMAÂă(10k) is $T_{\mathrm{G,PMMA}} = (115 \pm 5)°\mathrm{C}$ [19] . Both polymers were purchased from Polymer Standard Service Mainz (PSS-Mainz, Germany) with polydispersities of $M_w/M_n = 1.03$ for PS and of $M_w/M_n = 1.05$ in the case of PMMA. The surface tension of the PMMA-air interface is $\gamma_{\text{PMMA-air}} = (32 \pm 2)\,\mathrm{mN\,m^{-1}}$, that of the air-PS interface is $\gamma_{\text{PS-air}} = (31.5 \pm 0.2)\,\mathrm{mN\,m^{-1}}$, i.e. about 25 times larger than that of the buried PS-PMMA interface $\gamma_{\text{PS-PMMA}} = (1.25 \pm 0.07)\,\mathrm{mN\,m^{-1}}$ [19, 31].

The layered polymer system was prepared on silicon wafer cuts of about $(2 \times 2)\,\mathrm{cm^2}$ having crystal orientation of $\langle 100 \rangle$ and a natural oxide layer thickness of (2 ± 0.3)nm determined by ellipsometry (EP3, Accurion). Prior to coating, the silicon wafers were pre-cleaned with a fast CO_2 stream (Snow-Jet, Tectra) and then sonicated in ethanol, acetone and toluene. After each sonication step the silicon wafers were blow dried with compressed nitrogen gas. As a last cleaning step, residual hydrocarbons were etched away by a $30\,\mathrm{min}$ dip in Piranha etch (fresh $50 : 50$ mixture of sulphuric acid and hydrogen peroxide (30%)) followed by a thorough rinse with hot ultrapure water [32].

To prepare layered polymer films onto such a pre-cleaned wafer cut, first PMMA films were spin-coated from toluene solution to a thicknesses of either $h^0_{\mathrm{PMMA}} = (111 \pm 4)\,\mathrm{nm}$ or $h^0_{\mathrm{PMMA}} = (219 \pm 7)\,\mathrm{nm}$. As PS can not be spin-coated directly on PMMA using solvents that provide sufficiently good surface quality, PS was first spin-coated from toluene solution on freshly cleaved Mica sheets with thicknesses varying between about $h^0_{\mathrm{PS}} = 2\,\mathrm{nm}$ and $h^0_{\mathrm{PS}} = 10\,\mathrm{nm}$. Subsequently, these PS layers were floated on ultrapure water and picked up from above with the PMMA coated silicon substrate. The thicknesses of the polymer films were determined by ellipsometry. In case of PMMA films this could be done using the thin film samples as described above. To measure the thickness of PS films, we spin coated PS films on cleaned silicon wafers using the same solvent concentrations and spinning parameter as on Mica.

The interfacial width w between the immiscible polymers PS and PMMA based on self-consistent field theory is $w = a/\sqrt{2\chi}$ with the Flory-Huggins interaction parameter χ and segment length a. Commonly reported values for PS/PMMA interfaces lie in the range $w = 2 \ldots 5\,\mathrm{nm}$ [33, 34] with a logarithmic dependence on film thickness [35]. This potentially affects the molecular roughness of the PS-PMMA interfaces.

The dewetting processes were typically monitored in situ by atomic force microscopy in soft tapping mode (AFM, Dimension Icon, fast scan, Bruker). For the various experimental runs, the imaging temperatures were in the range of $(120 - 130)°\mathrm{C}$ to adapt the dynamics of the system to the imaging speed of the AFM. The viscosity of PS in this temperature range varies between $\mu_{\mathrm{PS}} \approx 9.8\,\mathrm{MPa\,s}$

and ≈ 0.98 MPa s and between $\mu_{\mathrm{PMMA}} \approx 6.5$ MPa s and ≈ 0.71 MPa s in case of PMMA [36]. The resulting viscosity ratio of PS and PMMA thus is $\mu = 1.5$ for $T = 120\,^{\circ}$C and $\mu = 1.38$ for $T = 130\,^{\circ}$C [19, 37]. For a more uniform presentation, we will rescale the experimentally observed rupture-times to the time-scale at the temperature $T = 125\,^{\circ}$C, where the polymer viscosities are approximately $\mu_{\mathrm{PS}} \approx 2.7$ MPa s and $\mu_{\mathrm{PMMA}} \approx 1.9$ MPa s. Since the experiments are performed at different temperatures and thereby there is some uncertainty about the values of the viscosities and the viscosity ratio, we will use $\mu = 1$ with the time-scale set by μ_{PMMA} throughout in the simulations. We found that for $h_{\mathrm{PMMA}} \gg h_{\mathrm{PS}}$ this has a relatively small impact on the dynamics.

For some experiments the sample was quenched to room temperature at a desired dewetting stage and the frozen dewetting pattern at the PS-air interface was imaged by AFM with great accuracy. Additionally, the PS layer was removed by dipping the glassy polymer sample in a selective solvent (cyclohexane, Sigma Aldrich, Germany) for five seconds at $50\,^{\circ}$C and immediately blow-dried after removal from the solvent with a gentle stream of nitrogen gas. Subsequently, the formerly buried PS-PMMA interface was imaged and the profile aligned with that of the PS-air interface to obtain a full three dimensional image.

To infer length-scale information from the AFM measurements, for $\alpha \in \{\mathrm{PS},\mathrm{PMMA}\}$ we employ the power spectral density

$$\mathrm{PSD}_\alpha(t,k) = N^{-2}|\mathcal{F}[h_\alpha(t)]|^2(\boldsymbol{k}) \tag{2.6}$$

with $\mathcal{F}[h](\boldsymbol{k})$ the discrete Fourier transformation of a mesh function (AFM measurement or numerical solution) $h \in \mathbb{R}^{N\times N}$ with $h_{ij} = h(x_i, y_j)$. Note that the normalization and averaging over constant $k = |\boldsymbol{k}|$ leads to power spectral densities, where for normalized Gaussian noise ξ one has $N^{-2}|\mathcal{F}[\xi]|(k) \approx 1$. We often show power spectral densities as a function of wavelength $\lambda = 2\pi/k$.

2.3 Effective Interface Potential

Based on the dielectric properties of PS and PMMA, the Hamaker constant for the multi-layered system consisting of air-PS-PMMA can be calculated to

$$A = 1.49 \times 10^{-20}\,\mathrm{J}, \tag{2.7}$$

see [38, 39]. The calculation of the Hamaker constant assumes all media being dielectric with a single electronic absorption frequency of 3×10^{15} Hz [39, pg. 186]. The relative relative permittivities of air, PS, and PMMA are $\varepsilon_r = \{1.00059, 2.6, 2.6\}$ and the corresponding refractive indices are $n_r = \{1.00029, 1.5894, 1.4893\}$ [38], respectively. Note that several common assumptions are made for the computation of the Hamaker constant, e.g., dielectric properties of bulk samples are identical to those of thin films and the assumption of one common absorption frequency. This leads to a realistic uncertainty in the order of $\pm 0.4 \times 10^{-20}$ J. However, the positive Hamaker constant implies that a PS film on top of a PMMA substrate is spinodally unstable, leading to amplification of unstable eigenmodes, spinodal film break up, and hole growth. This process is described by an intermolecular potential appearing in the free energy (2.1a) of the form

$$\Phi(h) = -\frac{A}{12\pi h^2} + \frac{B}{h^n}. \tag{2.8}$$

Here, in addition to the Hamaker constant A in the destabilizing Van der Waals force, stabilizing intermolecular forces are encoded in B and $n > 2$, where commonly used integer values are $3 \leq$

$n \leq 8$ [40]. For a given potential minimum $\phi_* = -\min_h \Phi > 0$, the precursor thickness is

$$h_* = \sqrt{\frac{(n-2)A}{12n\pi\phi_*}}, \tag{2.9}$$

and does not affect the instability as long as h_{PS} is sufficiently large. The minimum of the effective interface potential is related to the spreading coefficient $S < 0$ by

$$\begin{aligned}\phi_* = -S &= \gamma_{\text{PS-air}} + \gamma_{\text{PS-PMMA}} - \gamma_{\text{PMMA-air}} \\ &= (0.7 \pm 0.1)\,\mathrm{mN\,m^{-1}},\end{aligned} \tag{2.10}$$

and is determined for the PS-PMMA system from the shape and contact angles of stationary lenses [19]. Combining the potential in (2.8) with the Hamaker constant (2.7) and the potential minimum gives the potential shown in Figure 3. Apparently, for moderate film thicknesses $h_{\mathrm{PS}} \geq 3\,\mathrm{nm}$ the impact of short-range part encoded in ϕ_*, n is negligible and the potential is dominated by destabilizing Van der Waals forces which drive the spinodal instability. Thus, to allow for nonlinear simulations on larger domains we choose a potential with $n = 4$ and reduced minimum $\phi_* = 0.07\,\mathrm{mN\,m^{-1}}$, see green curve in Figure 3.

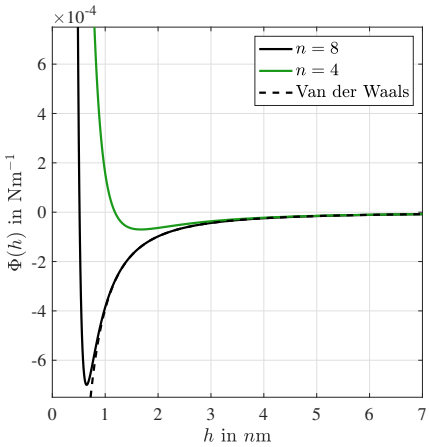

Figure 3: Effective interface potential Φ as a function of PS film thickness h_{PS}. The black line represents the full potential Φ with $n = 8$, while the black dashed line is only the long range Van der Waals term. The green curve shows the modified potential with $n = 4$ and a reduced minimum $\phi_* = (0.07)\mathrm{mN\,m^{-1}}$.

3 Results and Discussion

3.1 Evolution of experimental AFM profiles

We start the discussion by investigating the onset of the spinodal dewetting, as it is observed directly from the AFM measurements. When heating the prepared bilayer system to a temperature $T > T_{\mathrm{G},\alpha}$ where both polymers $\alpha = \{\mathrm{PS}, \mathrm{PMMA}\}$ are liquid, the surface topography evolves over time. As shown in the top panels of the exemplary time series in Figure 4, no visible topographic change is apparent in the experimental AFM profiles of the PS-air interface until small downward indentations start appearing rather late at $t = 990\,\mathrm{s}$. This is in contrast to the internal PS-PMMA interface depicted in the bottom panels of Figure 4, whose amplitude is visibly growing over time. Once the PS layer ruptures and PS-air and the PS-PMMA interface meet each other, holes are formed in the upper PS film and grow over time. This is faintly visible at the PS-air interface at $t = 990\,\mathrm{s}$ (dark spots, i.e.

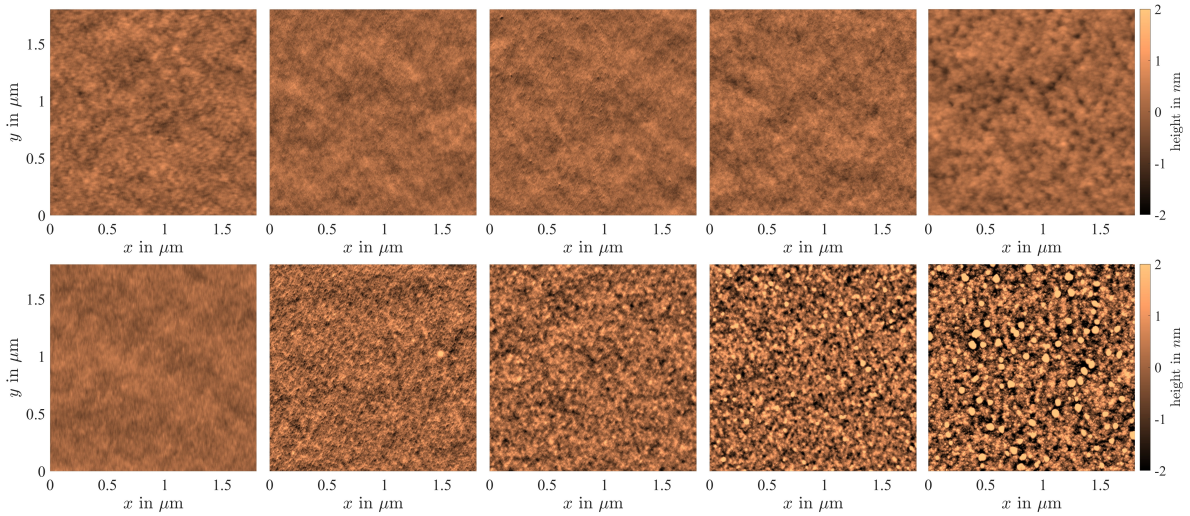

Figure 4: Ex situ AFM scan of the PS-air interface $h(t,\boldsymbol{x})-h^0$ (top) and of the PS-PMMA interface $h_{\mathrm{PMMA}}(t,\boldsymbol{x})-h^0_{\mathrm{PMMA}}$ (bottom) at increasing times $t=0\,\mathrm{s}, 90\,\mathrm{s}, 240\,\mathrm{s}, 525\,\mathrm{s}, 990\,\mathrm{s}$ from left to right. Experiment performed at $T=124\,^\circ\mathrm{C}$ with $h^0_{\mathrm{PS}}=6\,\mathrm{nm}$ and $h^0_{\mathrm{PMMA}}=111\,\mathrm{nm}$.

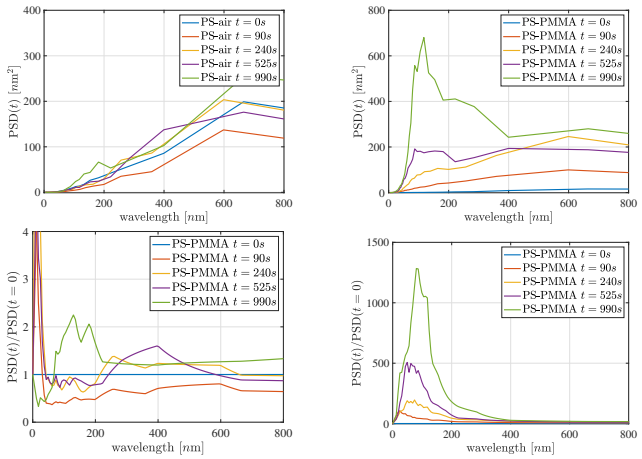

Figure 5: Experimental power spectral densities $\mathrm{PSD}(t,k)$ of AFM height data of PS-air interface (top left) and of PS-PMMA interface (top right) shown in Figure 4 and corresponding normalized power spectral density of PS-air (bottom left) and PS-PMMA (bottom right) interface. Normalization at t is taken with respect to the initial density at $t=0$, i.e., $\frac{\mathrm{PSD}(t,k)}{\mathrm{PSD}(0,k)}$ as a function of wavelength $\lambda=2\pi/k$.

downward deformation) and clearly visible at the PS-PMMA interface at $t=525\,\mathrm{s}$ and $990\,\mathrm{s}$ (bright spots, i.e. upward deformation).

To quantify the evolution of the roughness and the onset of spinodal dewetting we computed power spectral densities of the respective interfaces shown in Figure 4. While again no distinct wavelength can be identified from the PS-air interface in the upper left panel of Figure 5, the PS-PMMA interface in the upper right panel shows a clear growth over time and local maximum for $100\,\mathrm{nm}<\lambda<200\,\mathrm{nm}$.

While the maximum itself is clearly defined, the decay for larger wavelengths is rather slow since the initial data favor longer wavelengths. Thus we show the power spectral density at time t normalized with respect to the density at time $t=0$ in the lower panels of Figure 5. Now the existence of a fastest growing wavelength $\lambda_{\mathrm{exp}}=110\pm30\,\mathrm{nm}$ and a decay for larger wavelengths in the PS-PMMA interface becomes much more prominent. The corresponding power spectral density of the PS-air interface also shows a slight enhancement of amplitudes in the range $100\,\mathrm{nm}<\lambda<200\,\mathrm{nm}$ at the last time $t=990\,\mathrm{s}$, while the interpretation of the normalized power spectral density of the PS-air interfaces remains inconclusive for earlier times.

The preferred wavelength that can be observed at the PS-air interface just before film rupture agrees

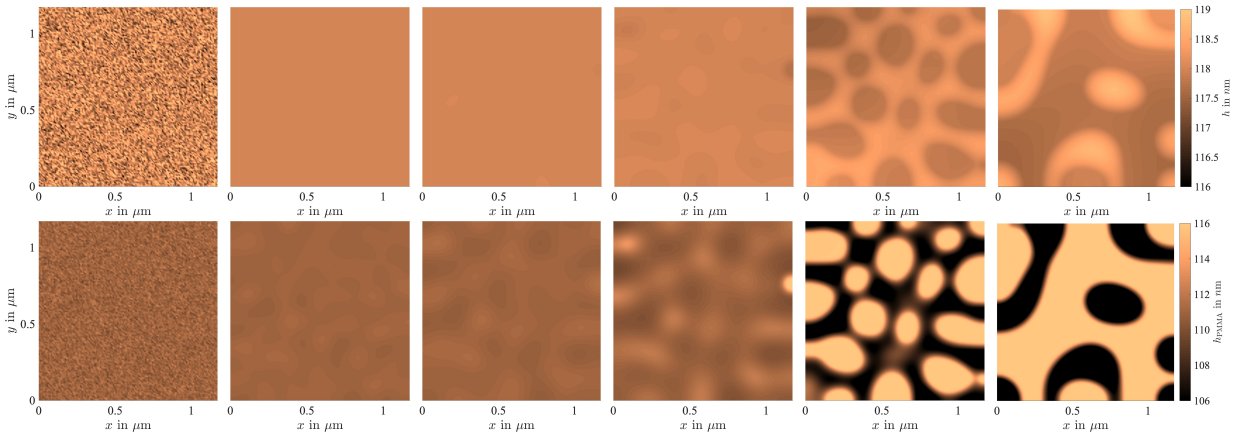

Figure 6: Numerical solutions $h(t,\boldsymbol{x}) = h_{\mathrm{PMMA}}(t,\boldsymbol{x}) + h_{\mathrm{PS}}(t,\boldsymbol{x})$ (upper row) and $h_{\mathrm{PMMA}}(t,\boldsymbol{x})$ (lower row) of the thin-film problem (2.1b) at times $t = \{0, 1.1, 10, 22, 33, 55\} \times 10^3$ s from left to right with **white noise** initial data. Initial film thicknesses are $h^0_{\mathrm{PS}} = 7$ nm and $h^0_{\mathrm{PMMA}} = 111$ nm, giving rise to $1/\sigma_u = 9400$ s and $\lambda_{\max} = 330$ nm.

with the preferred wavelength of the buried PS-PMMA interface and also the position of the holes right after their formation (as obtained by pair correlation function) agrees with this preferred wavelength obtained at the PS-PMMA interface. Therefore, based on the observation of a preferred wavelength and the agreement of the preferred hole distance with the preferred wavelength, we can conclude that it is in fact a spinodal process that leads to the evolution of the topography and finally to film rupture.

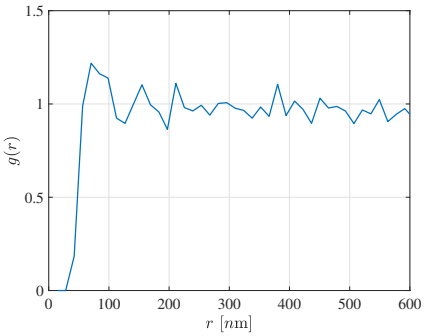

Figure 7: Pair correlation function $g(r)$ versus hole distance r (point data and smoothed profile) of the holes sites observed on the AFM profile of a PS-air interface. The AFM sample size is $2\,\mu\mathrm{m} \times 2\,\mu\mathrm{m}$ and 412 hole positions were identified and the average hole distance is $2\,\mu\mathrm{m}/\sqrt{412-1} = 99$ nm, consistent with the maxima in g at multiples of 80 ± 10 nm.

While the corrugations leading to film rupture are growing downwards on the PS-air interface and upwards on the buried PS-PMMA interface, the surface evolution seems synchronized in an anti-phase manner. From in-situ monitoring of both the topography and the material contrast (phase contrast) of an evolving PS-air surface as well as from aligning ex-situ measured PS-air and PMMA-PS interfaces, as shown in Figure 10, we can identify that holes appear in the valleys of the preferred wavelength, which proofs that the development of PS-air and PMMA-PS interfaces are anti-phase.

The observed spinodal wavelength increases for increasing PS film thickness, which was tested for PS film thicknesses in a range of $2\,\mathrm{nm} < h_{\mathrm{PS}} < 8.8\,\mathrm{nm}$. The experimentally determined wavelength is independent from the thickness of the liquid substrate provided it is sufficiently thick, which we also tested for PMMA films with thicknesses of $h^0_{\mathrm{PMMA}} = 111\,\mathrm{nm}$ (blue squares) and $h^0_{\mathrm{PMMA}} = 219\,\mathrm{nm}$ (red square) Figure 11(top). The experimentally accessible thickness range is limited to lower PS film thickness by the inability to preparation thinner PS films. Whereas, for PS films thicker than about $h^0_{\mathrm{PS}} = 8.8\,\mathrm{nm}$ a spinodal wavelength could not be detected reliably. The likely reason for that is that the driving van der Waals forces weaken for increasing film thickness leading to long spinodal

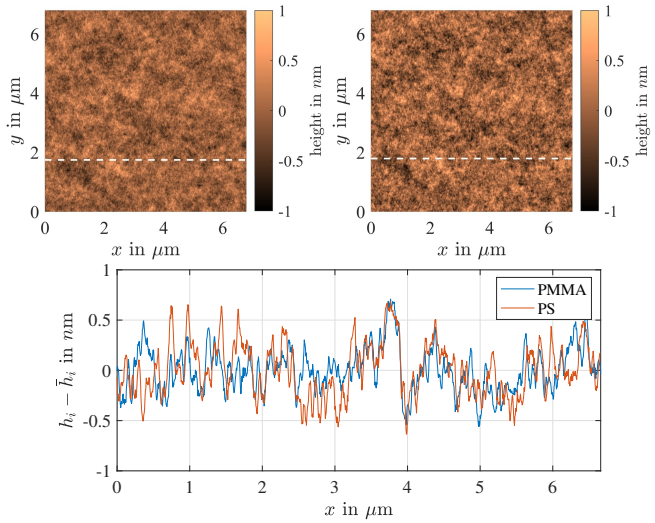

Figure 8: Experimental plane-fitted AFM images of the initial roughness of the PMMA layer after preparation (**left**) and of the same spot after floating a 7 nm thick PS layer on top (**middle**). Superimposed AFM cross sections at the dashed lines show the correlation of the interfaces (**right**). For better comparison the height average is subtracted from the AFM profiles.

rupture times and thus heterogeneous nucleation will eventually be faster. However, surface corrugations before hole breakup or between nucleated holes can still be observed for PS film thicknesses of $h^0_{\mathrm{PS}} = 8.8\,\mathrm{nm}$

The amplitude growth of the film thickness dependent preferred (spinodal) wavelength also leads to a characteristic rupture time that also increases with initially prepared PS film thickness h_{PS} Figure 11(bottom). Experimentally the breakup time is taken as the heating time required to detect the first hole in an AFM scan and therefore the breakup time might depend on scan size. However, as the scan areas are large compared to the spinodal wavelength and the statistics of hole sites is reasonably large this uncertainty is expected to be smaller that the uncertainty caused be the acquisition time for each AFM scan of around $4\,\mathrm{min}$.

3.2 Comparison with linear stability

Based on data extracted by power spectral density, the comparison of experimentally measured wavelengths compared to the expectation from the linear stability analysis is shown in Figure 11. We observe that the experimental wavelengths and rupture times increase with the polystyrene film thickness h^0_{PS}. However, the linear theory predicts both longer spinodal wavelengths and longer rupture times, i.e., the theoretical prediction of the spinodal wavelength is systematically larger by a factor of $1.5 - 2$. The weak dependence of the spinodal wavelength on the PMMA film thickness that is predicted by the linear stability analysis is experimentally confirmed, i.e., experimental determined wavelengths are independent on PMMA thickness withing the limits of measurement accuracy. The observed discrepancy between the predicted and the experimentally determined spinodal wavelength is unexpected as the linear stability analysis has been very successful in determining the experimentally observed spinodal wavelength when a thin polymer film dewets from a solid support[16, 41], which includes the applied computation of the Hamaker constant based on the approximation from [39]. The discrepancies in the rupture times have been already observed previously and it was argued that they are caused by thermal fluctuations, which can significantly speed-up the onset of the spinodal instability [42]. In the following we will thus discuss the possible origin of these discrepancies for liquid bilayers.

The discrepancy in the measured and theoretically expected rupture times and wavelengths can not

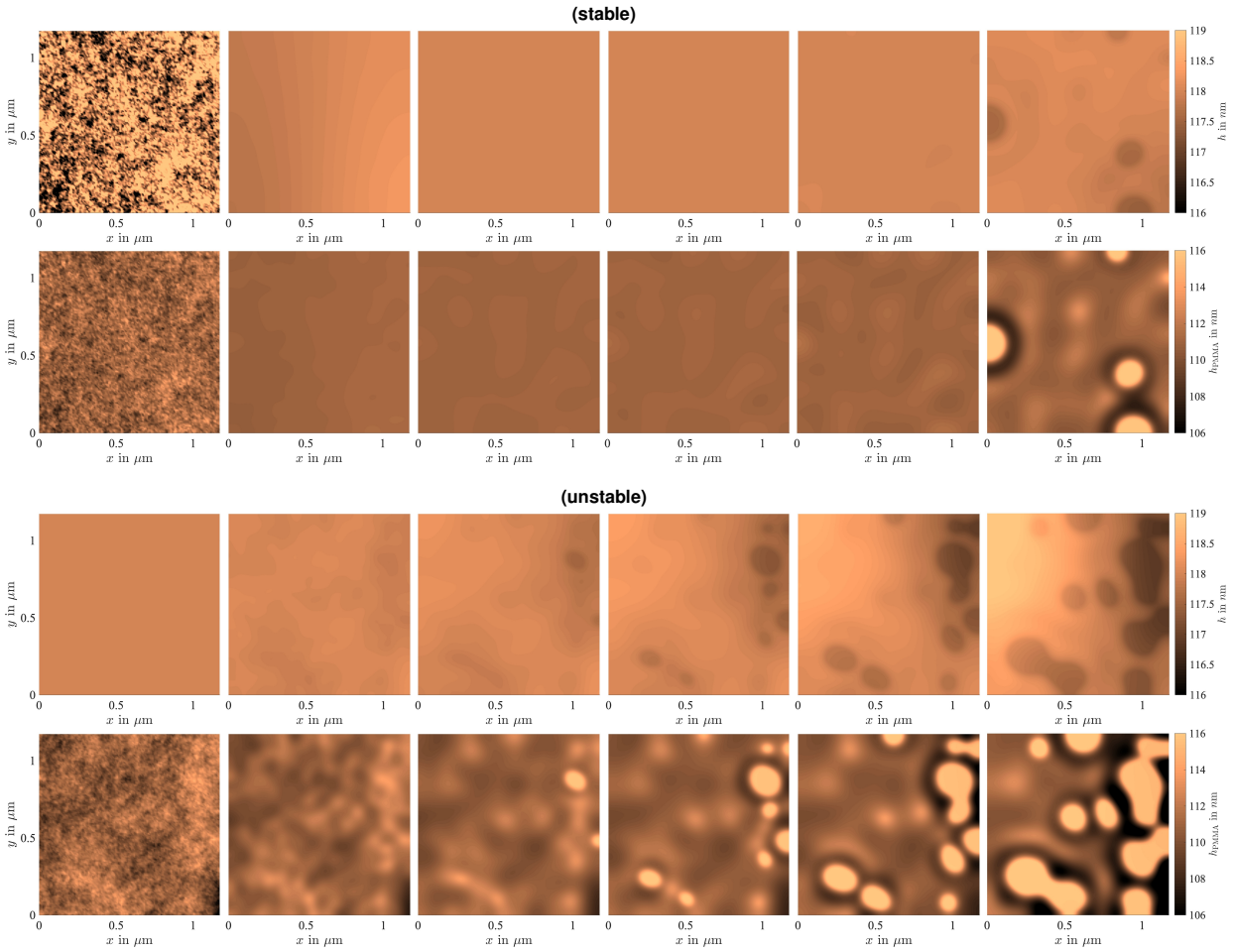

Figure 9: Numerical solutions with **colored noise** initiated with *stable* and *unstable* perturbations of flat layers. (**row 1,2**) **Stable** perturbation of flat layers at times $t = \{0, 0.67, 5.8, 12, 19, 32\} \times 10^3$ s increasing from left to right, where row 1 shows $h(t, \boldsymbol{x}) = h_{\mathrm{PMMA}}(t, \boldsymbol{x}) + h_{\mathrm{PS}}(t, \boldsymbol{x})$ and row 2 shows $h_{\mathrm{PMMA}}(t, \boldsymbol{x})$. (**row 3,4**) **Unstable** perturbation of flat layers at times $t = \{0, 0.14, 1.4, 2.8, 4.4, 7.2\} \times 10^3$ s from left to right, where row 3 shows $h(t, \boldsymbol{x}) = h_{\mathrm{PMMA}}(t, \boldsymbol{x}) + h_{\mathrm{PS}}(t, \boldsymbol{x})$ and row 4 shows $h_{\mathrm{PMMA}}(t, \boldsymbol{x})$. The color coding for the height is valid for each separate row. The film thicknesses for both, stable and unstable initial data, are $h^0_{\mathrm{PS}} = 7$ nm and $h^0_{\mathrm{PMMA}} = 111$ nm.

be explained using an uncertainty in the physical parameter of the polymer-polymer system: For the considered system at hand, a dependence of the spinodal wavelength on the exact viscosity or viscosity ratio is not expected from the linear theory. The specific choice of the intermolecular potential has a small effect on wavelength, i.e., for $h_{\mathrm{PS}} = 7$ nm the unstable wavelength $\lambda_{\max} = 330$ nm decreases at most by 5% upon different choices for the short-range potential and the rupture time decreases by up-to 25%. Any changes of the PS viscosity directly translate into a change of the time scale, which is certainly the greatest source of uncertainty for the rupture time. Nevertheless, for fixed μ_{PMMA} working with a viscosity ratio of $\mu = 1$ instead of $\mu = 1.4$ accounts for an error in the rupture time of less then 5%. Other dissipative effects such as slip at the polymer-polymer interface can further decrease the rupture time. For example, using $h_{\mathrm{PS}} = 7$ nm and an interfacial slip-length of $b_i = 10$ nm reduces the inverse of the maximally unstable eigenvalue from $1/\sigma_u = 9400$ s to $1/\sigma_u = 5800$ s and correspondingly reduces the rupture time. A certain uncertainty of the Hamaker constant and thus in the driving forces will directly impact the theoretically determined spinodal wavelength, whereas a Hamaker constant of $A = 3 \times 10^{-20}$, J that would be needed to explain the quantitative difference seems very unlikely. To the best of our knowledge the impact of the interfacial width $w = a/\sqrt{2\chi}$ on the spinodal instability of multilayered systems has not been discussed in literature but might contribute to the difference of predicted and observed wavelength.

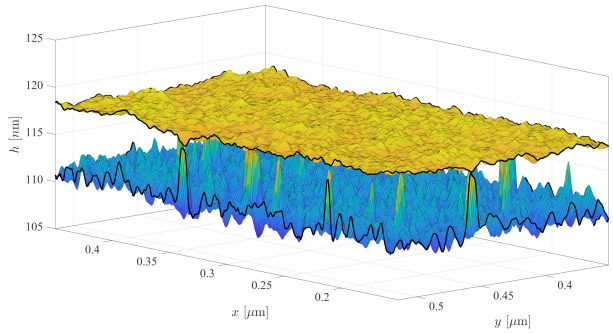

Figure 10: Aligned experimental AFM profiles of PS-air and PS-PMMA interfaces for $h^0_{\mathrm{PS}} = 7\,\mathrm{nm}$ and $h^0_{\mathrm{PMMA}} = 111\,\mathrm{nm}$ showing typical rupture sites at $t \sim 1.7 \times 10^3$ s when heated to $T = 128\,^\circ\mathrm{C}$.Downward indentations of the PS-air interface meet the upward indentations of the PS-PMMA interface leading to point rupture.

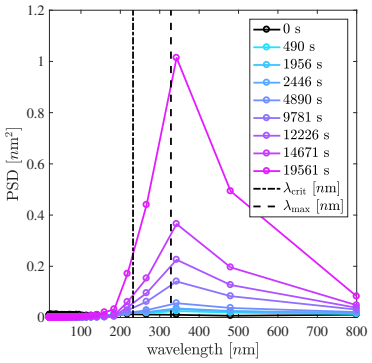

Figure 12: Power spectral density $\mathrm{PSD}(t, k = 2\pi/\lambda)$ of h_{PMMA} from the simulation shown in Figure 6 has a maximum that is compatible with $\lambda_{\max}$ from the linear stability.

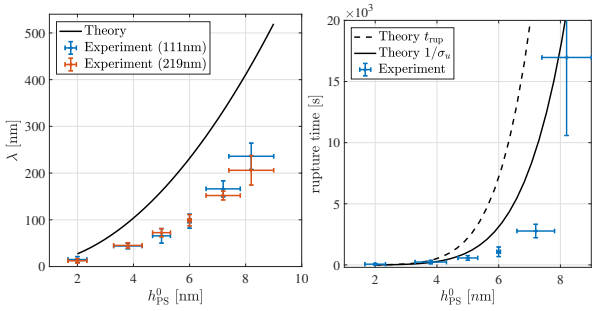

Figure 11: (**left**) Spinodal wavelength of PS(63k) with variable film thickness on PMMA(10k) having a film thickness of $111\,\mathrm{nm}$ (blue squares) and $219\,\mathrm{nm}$ (red squares) as determined by power spectral densities of the respective surfaces. The solid black line represents theoretical prediction from (2.5) for spinodal wavelength. The theoretical curves for a $111\,\mathrm{nm}$ and $219\,\mathrm{nm}$ PMMA thin film agree within the limits of plot visibility. (**right**) Spinodal breakup time determined by first appearance of hole. The rupture times were obtained for temperatures range from $120\,^\circ\mathrm{C}$ to $130\,^\circ\mathrm{C}$ and were re-scaled to a time-scale for a temperature of $125\,^\circ\mathrm{C}$ assuming a linear dependence between rupture time and polymer viscosity. The error bars are statistical errors including the uncertainty of an individual measurements. The breakup time for h_{PS} is taken out as hole breakup occurred by heterogeneous nucleation (uncorrelated holes sites) but a spinodal wavelength could be determined before hole breakup or in areas between holes.

3.3 Nonlinear evolution of spinodal dewetting

Roughness with white noise. The previously observed experimental results show the existence of a spinodal instability with a well-defined wavelength and rupture time. In addition to the physical parameters, the only choice left for the nonlinear evolution problem of PS-air and PS-PMMA interfaces

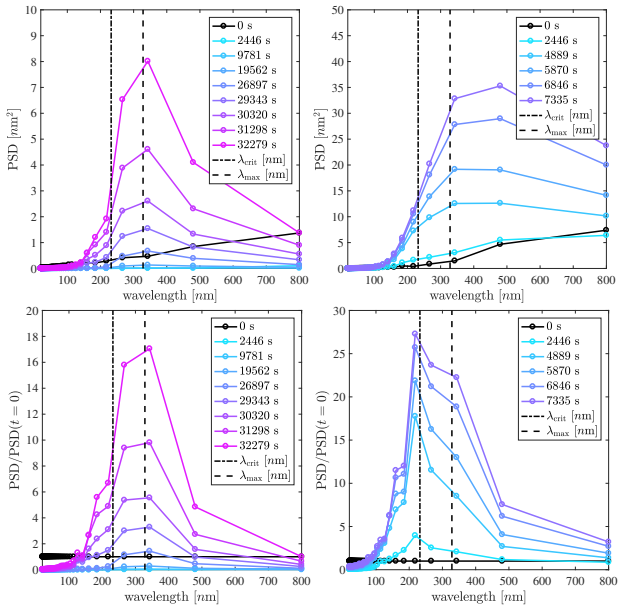

Figure 13: Power spectral density of h_{PMMA} at time t for numerical solutions with (**top left**) stable perturbation of flat film with appearance of first holes at $t = 10^4$ s and (**top right**) with unstable perturbations of flat film with first holes at $t = 0.5 \times 10^3$ s. (**bottom left**) Shows stable PSD corresponding to (first) but normalized w.r.t. the PSD at $t = 0$ and (**bottom right**) shows the unstable PSD corresponding to (second) but normalized w.r.t the PSD at $t = 0$.

(2.1b) is its initial data, i.e.,

$$h(t = 0, \boldsymbol{x}) = h^0 + \delta h\, \xi(\boldsymbol{x}),$$
$$h_{\mathrm{PMMA}}(t = 0, \boldsymbol{x}) = h^0_{\mathrm{PMMA}} + \delta h_{\mathrm{PMMA}}\, \xi_{\mathrm{PMMA}}(\boldsymbol{x}),$$

for $h = h_{\mathrm{PS}} + h_{\mathrm{PMMA}}$. In the following we investigate the impact of certain choices for the initial data. We restrict our considerations to small perturbations δh_α of a uniform thickness h^0_α, which might be suited to explain the discrepancy between experimental measurements and linear stability.

First, we simulate the effect of rough interfaces using normally distributed data $\xi_\alpha(\boldsymbol{x})$. An exemplary solution of (2.1b) is shown in Figure 6, where the initial film thickness is $h^0_{\mathrm{PS}} = 7\,\mathrm{nm}$ and is perturbed with white (Gaussian) noise with $\delta h = \delta h_{\mathrm{PMMA}} = 0.7\,\mathrm{nm}$ to resemble the initial roughness of the PS and PMMA layer. Similar to the experiment, one observes the growth of stronger deformations of the PS-PMMA interface and growth of smaller deformations of the PS-air surface. Most of the initial roughness is filtered out from the solution instantaneously, unlike in the experiment, where certain levels molecular roughness is present at all times. At time $t = 22 \times 10^3$ s the first hole becomes visible, which is compatible with the predicted rupture time of $1/\sigma_u = 9400$ s in Figure 11 from the linear theory, if one takes into consideration the logarithmic factor that incorporates the initial amplitude and the overlap with the unstable mode.

In agreement with the experimental results, the simulation results in Figure 6 show that the amplitude of the PS-air interface h remains comparably small $< 2\,\mathrm{nm}$ during the initial progression of the linear stability and is thereby comparable to the initial roughness of the PS-air interface . The main reason for the smallness of the PS-air interface deformation are the amplitudes of the unstable eigenmode $\boldsymbol{\chi}_u$, where due to the ratio of surface tensions $\gamma \ll 1$ we also have $|\chi^u_{\mathrm{h}}| \ll |\chi^u_{\mathrm{PMMA}}|$, as it can also be seen in the middle panel of Figure 2. Larger deformations of the PS-air interface can be observed in Figure 6 during the later dewetting process $t > 10^4$ s where holes grow and ultimately arrays of droplets are formed.

The corresponding power spectral density of the numerical solution with white noise initial data is shown in Figure 12. Since no preference is given to any wavelength, the fastest growing mode with

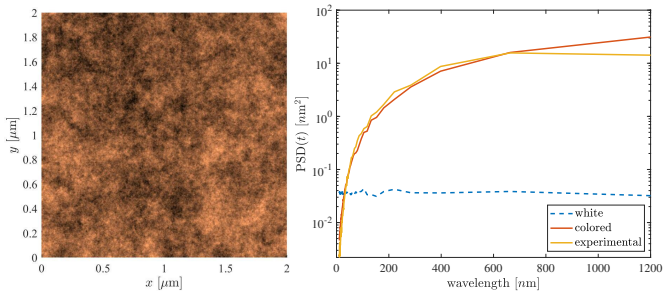

Figure 14: (**left**) Generated colored noise for $\rho = 1$ to be compared to white noise initial data in Figure 6 and the experimental noise in Figure 4. (**right**) Comparison of the log-PSD of the initial PS-PMMA interface experimentally determined by AFM (yellow solid line) versus generated interface with colored noise with exponent $\rho = 1$ (red line) and standard white noise (blue dashed line).

wavelength $\lambda = 350\,\text{nm}$ is clearly visible in the spectral density without any further normalization. This wavelength is compatible with fastest growing mode $\lambda_{\max} = 330\,\text{nm}$ for $h^0_{\text{PS}} = 7\,\text{nm}$ within the limited resolution in k-space due to the finite size of the computational domain.

Note that for stable perturbations the nonlinear simulations give wavelengths and rupture times which are compatible with the linear theory but considerably larger then the experimental observations.

Roughness with colored noise. As shown in Figure 4, the initially prepared PS-PMMA system features flat layers with a measurable molecular roughness of $R_q = 0.24 \pm 0.03\,\text{nm}$. Analyzing the initial AFM measurements of PS-air and PS-PMMA interface in Figure 4 and Figure 8 one observes an additional long-wavelength waviness of the profiles with typical wavelength of $\sim 1\mu$, m. Inspecting the corresponding power spectral densities in the upper panels Figure 5 then reveals that the initial roughness at $t = 0$ is not composed of white noise but is rather colored noise with a tendency for larger amplitudes at longer wavelength causing this “waviness”. Even more importantly, inspection of the cross-sections in the right panel of Figure 8 reveals that the initial roughness of the PS-PMMA and the PS-air interface is positively correlated, i.e., at last on a micrometer scale upward deformations of the PS-PMMA interface lead to upward deformations of the PS-air interface with $\langle (h - \langle h \rangle)(h_{\text{PMMA}} - \langle h_{\text{PMMA}} \rangle) \rangle \approx +\frac{1}{2}$ for the cross-sections shown in Figure 8. This immediately raises the question how of correlated noisy, rough or fluctuating interfaces affect in spinodal dewetting.

While it is beyond the scope of this paper to explore the impact of fluctuations on the spinodal dewetting as it has been done for single layer systems [27, 28], we will analyze here the impact of a colored, correlated initial roughness in the initial data of the thin-film problem on the observed rupture times and wavelengths. Therefore, we introduce the following model for initial data with colored noise

$$h(t{=}0, \boldsymbol{x}) = h^0 + \sum_{\boldsymbol{k}} \frac{\delta h^0}{|\boldsymbol{k}|^\rho}\, \xi(\boldsymbol{k}) \cos(k_x x) \cos(k_y y),$$

$$h_\alpha(t{=}0, \boldsymbol{x}) = h^0_\alpha + \sum_{\boldsymbol{k}} \frac{\delta h^0_\alpha}{|\boldsymbol{k}|^\rho}\, \xi_\alpha(\boldsymbol{k}) \cos(k_x x) \cos(k_y y),$$

for $\alpha = \text{PMMA}$ with $\boldsymbol{k} = (k_x, k_y) \in \frac{\pi}{L}(m_x, m_y)$ for $m_x, m_y = 1, ..., N$ and N the resolution of the AFM scan or the uniform mesh used for the solution of (2.1b). Here $\xi_\alpha(\boldsymbol{k})$ represent normally distributed random variables with the variance of $\sum_{\boldsymbol{k}} \xi_\alpha(\boldsymbol{k})/|\boldsymbol{k}|^\rho$ being one. In the right panel of Figure 14 a comparison of the initial experimental power spectral density of the PS-PMMA interface with the generated colored initial data is shown. Again, we see large wavelengths are favored and colored noise with $\rho = 1$ describes the initial data much better than white noise with $\rho = 0$. The left panel of Figure 14 also shows the corresponding generated noisy initial height h_{PMMA}, which can be

compared to the initial experimental profiles in Figure 4 or that in Figure 8. Compared to the previous white noise used in Figure 6, the colored noise is apparently a much better approximation of the experimental data. However, unlike in the experiment, short wavelengths will be quickly damped out during the nonlinear evolution due to surface tension so its impact on the nonlinear dynamics needs to be seen.

While ξ_α are uncorrelated for different $\boldsymbol{k}$, we are going to consider the case where $\xi_\alpha(\boldsymbol{k}) = \xi(\boldsymbol{k})$, i.e., the fluctuations of the PS-air and PS-PMMA interface are correlated or anticorrelated for each $\boldsymbol{k}$ depending on the signs δh_α. The reason to consider correlated noise is twofold: Firstly, inspection of cross section of the initial experimental noise in the right panel of Figure 8 suggest a positive correlation between the PS-PMMA and the PS-air interface deformation, i.e., at least for large wavelength the PS-air interface appears to follow the corrugations of the PS-PMMA interface. Secondly, selecting correlated (anticorrelated) colored noise allows us to select random initial data which, for each separate $\boldsymbol{k}$ lie on the stable or unstable branch of the dispersion relation if δh_α are proportional to the eigenvectors $\chi_\alpha^{s,u}$, respectively.

In accordance to the solution of the linear stability and the associated eigenvalue problem shown in Figure 2, we choose initial data on the stable and unstable branch via

$$\begin{aligned} \textbf{stable:} \quad & \delta h^0 = 1.2\,\text{nm}, && \delta h^0_{\text{PMMA}} = 1.2\,\text{nm}, \\ \textbf{unstable:} \quad & \delta h^0 = 0, && \delta h^0_{\text{PMMA}} = 1.2\,\text{nm}, \end{aligned}$$

where $\delta h^0 = \delta h^0_{\text{PMMA}} + \delta h^0_{\text{PS}}$, which is a sufficiently good approximation to the stable and unstable eigenvector for sufficiently large k. The values of $\delta h^0, \delta h$ are choosen to roughly match the observed variations in the experimental initial profiles and should, according to (2.5d), enter logarithmically into the rupture time t_{rup}. We choose the initial data on the stable and on the unstable branch of the dispersion relation in order to explore the impact on rupture times and wavelengths.

The resulting nonlinear simulations with colored noise and perturbed with stable and unstable amplitudes are shown in Figure 9. The stable perturbations shown in the upper two rows quickly die out for all length scales on both PS-air and PS-PMMA interface for early times, are then amplified again, finally leading to rupture at the last image at $t = 32 \times 10^3$ s. Note this takes slightly longer compared to the initial data which is perturbed by white noise shown in Figure 6, where the rupture occurs at $t = 22 \times 10^3$ s. On the contrary, for the unstable initial data shown in the lower two rows of Figure 9 the initial long-wavelength perturbations for $\lambda \geq \lambda_{\text{crit}}$ persist and are amplified exponentially with time. This leads to a much smaller rupture time $t_{\text{rup}} = 1.4 \times 10^3$ s, i.e., about 20$\times$ faster than for stable perturbations. Note this rupture time for $h^0_{\text{PS}} = 7$ nm is closer to the experimental observations shown in the right panel of Figure 11 since the overlap with the unstable mode is much larger. More importantly, since the initial perturbation is not damped at small times, the solution are entering the nonlinear regime of the spinodal instability, which should further decrease the observed rupture time.

In Figure 13 we show the power spectral density for the stable and unstable perturbed initial data with colored noise. For stable perturbations, the power spectral density shows first a fast decay of the initial perturbation which is then amplified over time and leads to rupture at $t_{\text{rup}} = 32 \times 10^3$ s. Due to the initial decay the rather strong initial perturbation falls back into a linearly small perturbation and thereby the fastest growing mode can fully develop and is visible in both, the power spectral density and the normalized power spectral density. The fastest growing wavelength $\lambda = 350$ nm observed in both left panels of Figure 13 is again compatible with $\lambda_{\max} = 330$ nm from linear theory. For unstable perturbations, the power spectral density immediately grows in time. Due to the initially larger amplitude of larger wavelength the power spectral density here shows a much larger maximum at $\lambda = 500$ nm at $t = 2648$ s which also has a large width at half height compared to the stable initial

data. Very likely this is due to the fact that the initial data start already in the nonlinear regime and the most unstable perturbation does not have enough time to grow out of the initial data. Notably, if the amplification is normalized with respect to the initial amplitude of the PSD, then the resulting maximum gives a significantly lower maximum in the PSD close to the critical wavelength $\lambda_{\mathrm{crit}} = 230\,\mathrm{nm}$, which is probably caused mainly by the nonlinear amplification of the initial perturbation in the unstable regime.

This shows that an indirect identification of the spinodal wavelength from PSD in the presence of colored noise and fluctuations requires a careful treatment of the initial state, as otherwise one might identify systematically lower or higher wavelengths. We observe considerable differences between the wavelengths measured from power spectral densities in the stable $\lambda = 350\,\mathrm{nm}$ and in the unstable $\lambda = 250\,\mathrm{nm}$ case.

4 Conclusion and outlook

We compared AFM-based experimental observations and theoretical prediction of the spinodal instability of a polymer-polymer system. While observations of wavelengths and rupture times clearly support the theoretical expectations for the the dependence of the spinodal instability on film thickness, experimental values are somewhat smaller compared to the prediction by linear theory. Observing that the initial roughness is both colored and correlated, we performed an investigation on the qualitative behavior of such initial data. While stable initial data give wavelength and rupture time mostly compatible with the linear theory, unstable perturbations produce smaller wavelength and considerably faster rupture time.

It remains a question which type of initial condition, i.e. stable or unstable, is more realistic for the experimental polymer-polymer system. The fact that we observe a positive correlation at longer wavelengths would speak for the stable case. The fact that the experimentally observed breakup times and wavelength are smaller than the theoretical prediction bears some resemblence to our observations for the unstable case. Concerning the positive correlation, it should also be noted here that for the breakup time not the correlation on the micrometer scale but the correlation of the interfaces at the unstable wavelength $\lambda \approx \lambda_{\mathrm{max}}$ is relevant. In this sense the question cannot be answered definitely and the resulting uncertainty in the rupture times emphasizes the strong influence of fluctuations, noise and roughness on the spinodal dewetting. These observations definitely call for an extension of the current theory for polymer-polymer dewetting and the inclusion of thermal fluctuations.

Another aspect that might be useful in distinguishing the impact of correlation and noise is that both pathways would have an impact on the subsequent pattern formation process. Similar to dewetting from a solid substrate, we observe for a narrow range of polystyrene film thicknesses the characteristic dewetting with satellite hole formation, see Figure 15.

References

[1] Alexander Oron, Stephen H Davis, and S George Bankoff. Long-scale evolution of thin liquid films. *Reviews of modern physics*, 69(3):931, 1997.

[2] Chun Huh and Laurence E Scriven. Hydrodynamic model of steady movement of a solid/liquid/fluid contact line. *Journal of colloid and interface science*, 35(1):85–101, 1971.

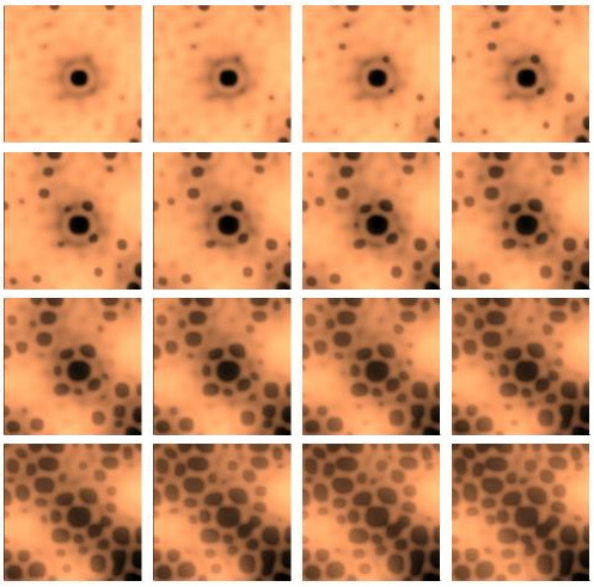

Figure 15: Characteristic satellite hole formation for film thicknesses h^0_{PS} between spinodal and heterogeneous nucleation.

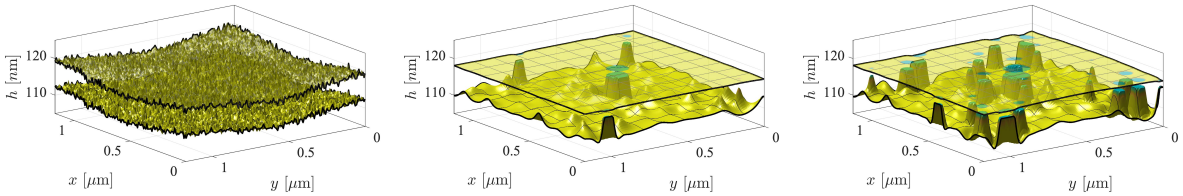

Figure 16: Numerical solution profiles of PS-air and PS-PMMA interface for $h^0_{\mathrm{PS}} = 7\,\mathrm{nm}$ and $h^0_{\mathrm{PMMA}} = 111\,\mathrm{nm}$ $t = \{0, 3.38, 3.66\} \times 10^4$ s.

[3] Jacco H Snoeijer and Bruno Andreotti. Moving contact lines: scales, regimes, and dynamical transitions. *Annual review of fluid mechanics*, 45:269–292, 2013.

[4] Richard V Craster and Omar K Matar. Dynamics and stability of thin liquid films. *Reviews of modern physics*, 81(3):1131, 2009.

[5] Pierre-Gilles De Gennes. Wetting: statics and dynamics. *Reviews of modern physics*, 57(3):827, 1985.

[6] Daniel Bonn, Jens Eggers, Joseph Indekeu, Jacques Meunier, and Etienne Rolley. Wetting and spreading. *Reviews of modern physics*, 81(2):739, 2009.

[7] J. Lal, L. B. Lurio, D. Liang, S. Narayanan, S. B. Darling, and M. Sutton. Universal dynamics of coarsening during polymer-polymer thin-film spinodal dewetting kinetics. *Phys. Rev. E*, 102:032802, Sep 2020.

[8] Günter Reiter. Dewetting of thin polymer films. *Physical review letters*, 68(1):75, 1992.

[9] Ralf Seemann, Stephan Herminghaus, and Karin Jacobs. Dewetting patterns and molecular forces: A reconciliation. *Physical Review Letters*, 86(24):5534, 2001.

[10] R Xie, Alamgir Karim, Jack F Douglas, Charles C Han, and Robert A Weiss. Spinodal dewetting of thin polymer films. *Physical Review Letters*, 81(6):1251, 1998.

[11] Andrey Pototsky, Michael Bestehorn, Domnic Merkt, and Uwe Thiele. Alternative pathways of dewetting for a thin liquid two-layer film. *Physical Review E*, 70(2):025201, 2004.

[12] Andrey Pototsky, Michael Bestehorn, Domnic Merkt, and Uwe Thiele. Morphology changes in the evolution of liquid two-layer films. *The Journal of chemical physics*, 122(22):224711, 2005.

[13] Dipankar Bandyopadhyay, Ritesh Gulabani, and Ashutosh Sharma. Instability and dynamics of thin liquid bilayers. *Industrial & engineering chemistry research*, 44(5):1259–1272, 2005.

[14] LS Fisher and AA Golovin. Nonlinear stability analysis of a two-layer thin liquid film: Dewetting and autophobic behavior. *Journal of colloid and interface science*, 291(2):515–528, 2005.

[15] Ralf Seemann, Stephan Herminghaus, and Karin Jacobs. Gaining control of pattern formation of dewetting liquid films. *Journal of Physics: Condensed Matter*, 13(21):4925, 2001.

[16] Jürgen Becker, Günther Grün, Ralf Seemann, Hubert Mantz, Karin Jacobs, Klaus R Mecke, and Ralf Blossey. Complex dewetting scenarios captured by thin-film models. *Nature materials*, 2(1):59–63, 2003.

[17] Pierre-Gilles De Gennes, Françoise Brochard-Wyart, and David Quéré. *Capillarity and wetting phenomena: drops, bubbles, pearls, waves*. Springer Science & Business Media, 2013.

[18] Stefan Bommer, Florian Cartellier, Sebastian Jachalski, Dirk Peschka, Ralf Seemann, and Barbara Wagner. Droplets on liquids and their journey into equilibrium. *The European Physical Journal E*, 36(8):87, 2013.

[19] Dirk Peschka, Stefan Bommer, Sebastian Jachalski, Ralf Seemann, and Barbara Wagner. Impact of energy dissipation on interface shapes and on rates for dewetting from liquid substrates. *Scientific Reports*, 8(1):1–11, 2018.

[20] M. Sferrazza, M. Heppenstall-Butler, R. Cubitt, D. Bucknall, J. Webster, and R. A. L. Jones. Interfacial instability driven by dispersive forces: The early stages of spinodal dewetting of a thin polymer film on a polymer substrate. *Phys. Rev. Lett.*, 81:5173–5176.

[21] Dipankar Bandyopadhyay and Ashutosh Sharma. Nonlinear instabilities and pathways of rupture in thin liquid bilayers. *The Journal of Chemical Physics*, 125(5):054711, 2006.

[22] Sebastian Jachalski, Dirk Peschka, Andreas Münch, and Barbara Wagner. Impact of interfacial slip on the stability of liquid two-layer polymer films. *Journal of Engineering Mathematics*, 86(1):9–29, 2014.

[23] Krassimir D Danov, Vesselin N Paunov, Norbert Alleborn, Hans Raszillier, and Franz Durst. Stability of evaporating two-layered liquid film in the presence of surfactantâĂŤi. the equations of lubrication approximation. *Chemical engineering science*, 53(15):2809–2822, 1998.

[24] George Karapetsas, Richard V Craster, and Omar K Matar. Surfactant-driven dynamics of liquid lenses. *Physics of Fluids*, 23(12):122106, 2011.

[25] Robert Huth, Sebastian Jachalski, Georgy Kitavtsev, and Dirk Peschka. Gradient flow perspective on thin-film bilayer flows. *Journal of Engineering Mathematics*, 94(1):43–61, 2015.

[26] P. Lambooy, K. C. Phelan, O. Haugg, and G. Krausch. Dewetting at the liquid-liquid interface. *Phys. Rev. Lett.*, 76:1110–1113, Feb 1996.

[27] Benny Davidovitch, Esteban Moro, and Howard A Stone. Spreading of viscous fluid drops on a solid substrate assisted by thermal fluctuations. *Physical Review Letters*, 95(24):244505, 2005.

[28] Günther Grün, Klaus Mecke, and Markus Rauscher. Thin-film flow influenced by thermal noise. *Journal of Statistical Physics*, 122(6):1261–1291, 2006.

[29] Stefan Bommer, Florian Cartellier, Sebastian Jachalski, Dirk Peschka, Ralf Seemann, and Barbara Wagner. Droplets on liquids and their journey into equilibrium. *The European Physical Journal E*, 36(8):87, 2013.

[30] Daniel Arndt, Wolfgang Bangerth, Bruno Blais, Thomas C Clevenger, Marc Fehling, Alexander V Grayver, Timo Heister, Luca Heltai, Martin Kronbichler, Matthias Maier, et al. The deal. ii library, version 9.2. *Journal of Numerical Mathematics*, 1(ahead-of-print), 2020.

[31] Souheng Wu. Surface and interfacial tensions of polymer melts. ii. poly (methyl methacrylate), poly (n-butyl methacrylate), and polystyrene. *The Journal of Physical Chemistry*, 74(3):632–638, 1970.

[32] Matthias Lessel, Oliver Bäumchen, Mischa Klos, Hendrik Hähl, Renate Fetzer, Michael Paulus, Ralf Seemann, and Karin Jacobs. Self-assembled silane monolayers: an efficient step-by-step recipe for high-quality, low energy surfaces. *Surface and Interface Analysis*, 47(5):557–564, 2015.

[33] ML Fernandez, JS Higgins, J Penfold, RC Ward, C Shackleton, and DJ Walsh. Neutron reflection investigation of the interface between an immiscible polymer pair. *Polymer*, 29(11):1923–1928, 1988.

[34] DW Schubert and Manfred Stamm. Influence of chain length on the interface width of an incompatible polymer blend. *EPL (Europhysics Letters)*, 35(6):419, 1996.

[35] Michele Sferrazza, C Xiao, Richard Anthony Lewis Jones, David G Bucknall, J Webster, and J Penfold. Evidence for capillary waves at immiscible polymer/polymer interfaces. *Physical review letters*, 78(19):3693, 1997.

[36] Ranxing N Li, Fei Chen, Chi-Hang Lam, and Ophelia KC Tsui. Viscosity of PMMA on silica: Epitome of systems with strong polymer–substrate interactions. *Macromolecules*, 46(19):7889–7893, 2013.

[37] Fabio Zulli, Marco Giordano, and Laura Andreozzi. Chain-length dependence of relaxation and dynamics in poly (methyl methacrylate) from oligomers to polymers. *Macromolecules*, 51(5):1798–1810, 2018.

[38] David R Lide. *CRC Handbook of Chemistry and Physics: A Ready-reference Book of Chemical and Physical Data*. CRC Press, 1995.

[39] Jacob N Israelachvili. *Intermolecular and surface forces*. Academic press, 2011.

[40] Andrea L Bertozzi, Günther Grün, and Tom P Witelski. Dewetting films: bifurcations and concentrations. *Nonlinearity*, 14(6):1569, 2001.

[41] Ralf Seemann, Stephan Herminghaus, and Karin Jacobs. Dewetting patterns and molecular forces: A reconciliation. *Physical Review Letters*, 86(24):5534, 2001.

[42] Renate Fetzer, M Rauscher, R Seemann, K Jacobs, and K Mecke. Thermal noise influences fluid flow in thin films during spinodal dewetting. *Physical Review Letters*, 99(11):114503, 2007.